Monitoring Active Sites for Hydrogen Evolution Reaction at Model Carbon Surfaces

Regina M. Kluge[a,‡], Richard W. Haid[a,‡], Ifan E. L. Stephens[b], Federico Calle-Vallejo[c], and Aliaksandr S. Bandarenka*[a,d]

Carbon is ubiquitous as an electrode material in electrochemical energy conversion devices. If used as support material, the evolution of H_2 is undesired on carbon. However, recently carbon-based materials are of high interest as economic and eco-conscious alternative to noble metal catalysts. The targeted design of improved carbon electrode materials requires atomic scale insight into the structure of the sites that catalyse H_2 evolution. This work demonstrates that electrochemical scanning tunnelling microscopy under reaction conditions (n-EC-STM) can monitor active sites of highly oriented pyrolytic graphite for the hydrogen evolution reaction. With down to atomic resolution, the most active sites in acidic medium are pinpointed near edge sites and defects, whereas the basal planes remain inactive. Density functional theory calculations support these findings and reveal that only specific defects on graphite are active. Motivated by these results, the extensive usage of n-EC-STM on doped carbon-based materials is encouraged to locate their active sites and guide the synthesis of enhanced electrocatalysts.

1. Introduction

Carbon is the most common electrode material in electrochemical energy conversion devices. For instance, in water electrolysis, the role of carbon is a conductive and inexpensive support for platinum nanoparticles, which catalyse H_2 evolution.[1,2] Recently researchers have started to use carbon-based materials, particularly doped carbon, as a catalyst for H_2 evolution, rather than a support, by virtue of its low cost, stability and ability to yield large surface areas.[1] While in water electrolysis, H_2 is the desired product, there are far more devices where H_2 is undesired, including supercapacitors[3], batteries[4], CO_2 reducing and N_2 reducing[5] electrolysers. The identification of active sites would thus help to either support or suppress the evolution of hydrogen depending on the application.

In order to restrict the range of investigation, the focus of the present study on carbon-based catalysts will be set on graphitic materials, more precisely on highly ordered pyrolytic graphite (HOPG). HOPG can serve as a model system for more complex carbon-based materials such as graphene, carbon nanotubes or fullerenes in view of their similarities in structure and electrochemical behaviour.[6] Graphitic materials come with the widely exploited possibility to functionalize the carbon backbone with foreign heteroatoms such as nitrogen, sulphur, boron and other p-block elements.[7] In the past, carbon-based catalysts proved to be well-performing for the hydrogen evolution (HER)[8,9,10], oxygen reduction (ORR)[11,12,13], and oxygen evolution (OER)[14,15] reactions.

When examining the activity of graphitic materials, the distinction between basal and edge planes is of utmost importance.[16] An ideal basal HOPG surface exhibits neither edge planes nor dangling bonds, since the valences of the carbon atoms are satisfied. In a real system, however, structural disorder causes the appearance of edge planes and vacancies.[17] Basal and edge planes possess contrasting rates toward electrochemical reactions. The activity of the basal plane is small compared to the activity of the edge states.[16] Therefore, the basal plane activity was only measurable during a very short time scale.[18] Most authors ascribe the activity to sites departing from the basal planes. These contributions can be subdivided into active edge states[12,15,19,20,21], carbon vacancies[15,22] and deviations in ring structure[22,23]. In the case of heterogeneous doping, it is widely accepted that the introduction of p-block elements and metal atoms increases the number of active sites. However, the role of the nitrogen atom coordination[24] as well as the influence of metal atoms on adjacent carbon atoms[8,10] remains a matter of debate[13]. Apart from observing a direct relation between defects and activity, an accurate localization of active sites remains open for both pristine and doped carbon catalysts.

Addressing these ambiguities from the literature, we use the power of a conventional electrochemical scanning tunnelling microscope (EC-STM) to in-situ visualize active sites.[25] In this

[a] *Physics of Energy Conversion and Storage, Physik-Department, Technische Universität München, James-Franck-Strasse 1, 85748 Garching (Germany)*
[b] *Department of Materials, Imperial College London, Royal School of Mines, Prince Consort Rd, London, SW7 2AZ (UK)*
[c] *Departament de Ciència de Materials i Química Fisica & Institut de Química Teòrica i Computacional (IQTCUB), Universitat de Barcelona, Martí i Franqués 1, 08028 Barcelona (Spain)*
[d] *Catalysis Research Center TUM, Ernst-Otto-Fischer-Strasse 1, 85748 Garching (Germany)*
‡ RMK and RWH contributed equally to this work.
* corresponding author. E-mail: bandarenka@ph.tum.de
Electronic Supplementary Information (ESI) available: [details of any supplementary information available should be included here]. See DOI: 10.1039/x0xx00000x

study, we applied this technique on undoped HOPG under HER conditions. Outstandingly, with an improved resolution down to the atomic scale, we pinpoint the active sites to step edges and defects rather than defect-free terraces. Substantiating our experiments, we used density functional theory (DFT) calculations to determine the energetics of hydrogen adsorption at these sites. The results of our investigations can be used as guidelines to tune the structure of the carbon catalyst in order to either in- or decrease the HER activity, depending on the desired application. Our results are encouraging for the future application of the EC-STM technique to more complex systems, e.g., heterogeneously doped graphite, and to more complex reactions such as ORR and OER.

2. Methods

2.1 Experimental Details

The noise EC-STM (n-EC-STM) measurements were conducted with a MultiMode scanning probe microscope connected to a NanoScope III scan feedback controller and a Universal Bipotentiostat (Veeco Instruments). Tips were mechanically ripped off a Pt80Ir20 wire (GoodFellow, Ø 0.25mm) with a side cutter and insulated with Apiezon wax, leaving only the very end of the tip uncovered.[26] The HOPG sample (MikroMasch, spread 3.5°±1.5°) was prepared by removing its first layers with sticky tape and mounted between a stainless steel sample holder and a Teflon ring. The Teflon ring was subsequently filled in with the electrolyte, exposing a sample area of 0.28 cm^2. The electrolyte was prepared by diluting perchloric acid, $HClO_4$ (Merck Suprapur®, 70%) with ultrapure water (18.2 MΩ) from an Evoqua Ultra Clear 10TWF 30 UV (Evoqua, Germany) water purification system to a concentration of 0.1 M. The miniature electrochemical cell was completed by immersing the reference and counter electrodes into the electrolyte next to the STM tip and connecting them to the EC-STM system. A Pt wire (MaTecK, Ø 0.5mm, 99.99% purity) was employed as the reference electrode. The Pt quasi-reference electrode was chosen due to the limited dimensions of the cell. Although a direct comparison to e.g. the reversible hydrogen electrode (RHE) scale is not feasible, it has been proven reliable for EC-STM purposes.[25,27–30] A graphite rod (Goodfellow, Ø 0.5mm, 99.95% purity) was chosen as the counter electrode to avoid deposition of foreign materials on the surface that could act as active sites and falsify the measurement. In order to access electrochemical properties, cyclic voltammograms (CVs) were recorded using the above described setup. All measurements were recorded at room temperature, and the data were evaluated using the WSxM 5.0 Develop 9.4 software.[31] Measurements were frequency-filtered using the fast Fourier transform (FFT) procedure to increase the impact of the noise originating from the ongoing reaction. Note that after this transform, sites demonstrating a higher noise level in the as-recorded image will show a higher tunnelling current and therefore appear as bright white spots in the image. Tip potential and current set-point of each data set are given in Table S1 of the Supplementary Information.

2.2 Computational Details

The DFT calculations were made with the Vienna ab initio simulation package (VASP)[32], using the projector augmented-wave (PAW) method[33] and the revised Perdew-Burke-Ernzerhof (RPBE) exchange-correlation functional.[34] HOPG was modelled as a variety of pristine and defective graphene layers on two different unit cells ($cell_1$ and $cell_2$, see Figures S5-S11 in the Supplementary Information). $Cell_1$ consists of the 'traditional' honeycomb structure consisting of carbon atoms arranged as hexagons, whereas $cell_2$ contains also pentagons, heptagons and octagons. In the geometry optimizations, all carbon atoms and the hydrogen adsorbates were allowed to relax in all directions using the conjugate-gradient optimization scheme until the maximal force on any atom was below 0.01 eV $Å^{-1}$. We used a plane-wave cut-off of 500 eV and k_BT = 0.001 eV with Gaussian smearing, and the total energies were extrapolated to 0 K. Monkhorst-Pack meshes of 4×3×1 and 3×3×1 ensured convergence of the adsorption energies within 0.05 eV for $cell_1$ and $cell_2$.[35] The vacuum layer between periodically repeated images in the vertical direction was larger than 14 Å and dipole corrections were included. H_2(g) was calculated in boxes of 15× 15×15 $Å^3$ using k_BT = 0.001 eV, Gaussian smearing and sampling the Γ point only. The computational hydrogen electrode was used to describe the energetics of proton-electron pairs, so that 0.5 $\mu(H_2) = \mu(H^+ + e^-)$.[36] The free energies of adsorption of *H ($^* + H^+ + e^- \rightarrow {}^*H$, where * is a free active site) were calculated as: $\Delta G_H \approx \Delta E_{DFT} + \Delta ZPE - T\Delta S$, where ΔE_{DFT} is the DFT adsorption energy of *H, ΔZPE is the zero-point energy change and TΔS is the entropy change at 298.15 K. The ZPE of *H is 0.29 eV on pristine graphene and that of H_2(g) is 0.28 eV, both calculated with DFT within the harmonic oscillator approximation. The TS correction including only the vibrational entropy for *H is just 2 meV on pristine graphene (also calculated with DFT), whereas the TS correction including all contributions is 0.40 eV for H_2(g).[37] The HER overpotentials (η_{HER}) were calculated based on the largest positive free energies of reaction: $\eta_{HER} = \pm\Delta G_H / e^-$, where e^- is the charge of an electron, and the sign is dictated by the adsorption energy: if it is exothermic, the sign is negative, whereas if endothermic, the sign is positive.[38] We evaluated the adsorption of atomic hydrogen on site I in Figure 5 with and without dispersion corrections[39] and obtained in both cases -0.26 eV, which suggests that dispersion corrections are not necessary in this case. We also evaluated the contributions of water solvation to the adsorption energies of hydrogen by means of an implicit solvation method.[40] The hydrogen adsorption energy of site I in Figure 5 is -0.27 eV, which suggests that solvation corrections are not necessary in this case. This agrees well with recent micro-solvation works reporting that H_2O, whether explicitly or implicitly incorporated in the

calculations, does not appreciably stabilize *CH, *CH_2 and *CH_3 adsorption energies, which is justified by the scarce polarity of C-H bonds.[41]

3. Results

The differentiation between basal and edge planes of HOPG is of importance considering their electrocatalytic activity.[16] Thus, scanning tunnelling microscopy (STM) recorded in air was performed to visualize the surface and is shown in Figure S1 of the Supplementary Information. A large-scale image where both basal and edge planes can be observed (Figure S1a) and an image resolving the typical honeycomb lattice of graphite are given (Figure S1b). In the following, basal and edge planes will be referred to as 'terraces' and 'steps'.

In order to probe the electrochemical properties of the material in 0.1 M $HClO_4$, cyclic voltammograms (CVs) were recorded; a typical one appears in Figure 1a. Note that the voltammograms were recorded against a Pt quasi-reference electrode in the EC-STM cell exposed to air and using a carbon-based counter electrode (see methods part 2.1 for more details). The current is normalized to geometric surface area. The features occurring can be roughly divided into three regions: one mainly related to the HER, the double layer (DL) region and the OER. In contrast to conventional metal-based catalysts, the DL possesses a lower capacitance and does not show any signs of oxide formation and reduction.[42] Taking a closer look at the HER-region, different features can be seen and are enlarged in Figure 1b. Going from higher to lower potentials, we ascribed them to: (IV) double layer charging-discharging, (III) a pair of peaks related to a quinone–hydroquinone transition[8,43],(II) a shoulder caused by the reduction of adsorbed (during OER) oxygen molecules[44], and (I) the quasi-exponential increase of current due to H_2 evolution. Dangling bonds at the edge sites of HOPG are likely to be passivated by oxygen-containing functional groups.[17] Therefore, in order to exclude the influences of such surface oxides on the measurement, we choose the most negative potential window (I) to allow for the HER to occur during the later n-EC-STM measurements (reaction 'on'). At these potentials, we assume all dangling bonds to be passivated with hydrogen only. To turn the reaction 'off', we set the potential within the DL region (IV).

Having determined the potential windows to turn the HER 'on' and 'off' in the n-EC-STM set-up, we discuss the results of the n-EC-STM measurements. Details on the functionality and possible application of n-EC-STM can be found elsewhere.[25,27–30] Please also refer to further explanations given in Section S3 of the Supplementary Information. In short, EC-STM differs from the conventional STM such that an electrolyte serves as a tunnelling medium. By controlling the sample potential, chemical reactions can or cannot occur at the electrode-electrolyte interface (reaction 'on'/'off'). It is known that the recorded tunnelling current depends exponentially on the (effective) tunnelling barrier and its properties.[45,46,47] Thus, abrupt changes in the tunnelling current are a direct

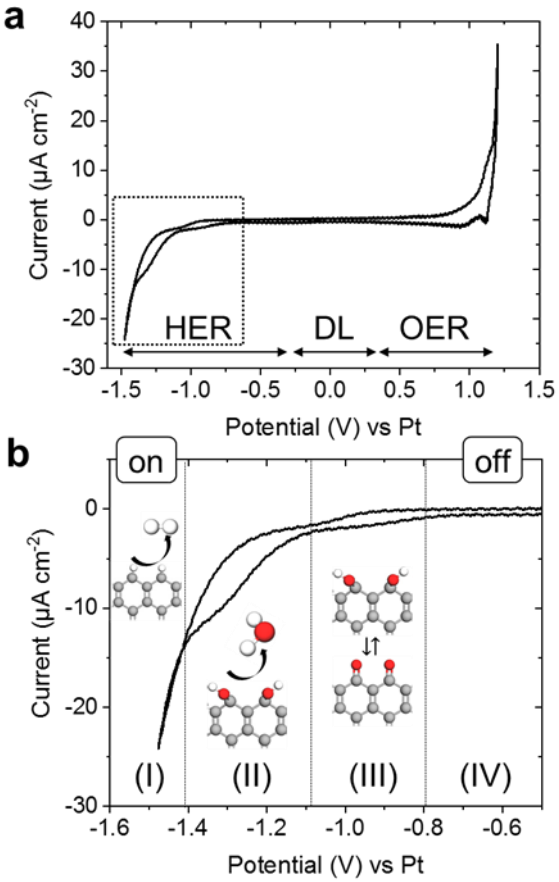

Figure 1. a, CV of HOPG as recorded in 0.1 M $HClO_4$ against a Pt quasi-reference. The CV can be divided into a double layer (DL) region of low capacitance, as well as the HER and OER occurring at the lower and higher potential ends, respectively. b, Enlarged view of the HER region showing some distinct features. From high to low potentials, there is (IV) a part of the DL, (III) a double peak that can be ascribed to a quinone–hydroquinone transition, (II) a shoulder that can be related to the reduction of adsorbed oxygen molecules, and (I) a peak related to H^+ reduction to H_2. During the subsequent n-EC-STM experiments, region (IV) will be ascribed to the conditions when no reaction takes place ('off') and region (I) to the one where the actual HER occurs ('on').

consequence of abrupt changes in the tunnelling barrier. An ongoing reaction continuously influences the structure and composition of the tunnelling medium (cf. Figure S2 of the Supplementary Information) and, thus, also the tunnelling barrier.[45,46,48] Therefore, the STM signal detected over catalytically active sites is destabilized compared to inactive sites, and shows a higher noise level. If the reaction is inhibited ('off'), the STM signal is stable. The difference in the noise level of active and inactive areas has been established for the in-situ identification of active centres.[25,27–30] Figure 2 schematizes an n-EC-STM measurement using a graphitic electrode material, where the basal plane is interrupted by a monoatomic step edge. The active carbon atoms are exemplarily located at the step edge and coloured in yellow. When the sample potential is set such that a reaction on the surface is hindered (Figure 2a), a 'conductivity map' of the surface is recorded, which can in this case be related to the height profile of the sample. If the potential is set such that the reaction takes place, an increase in

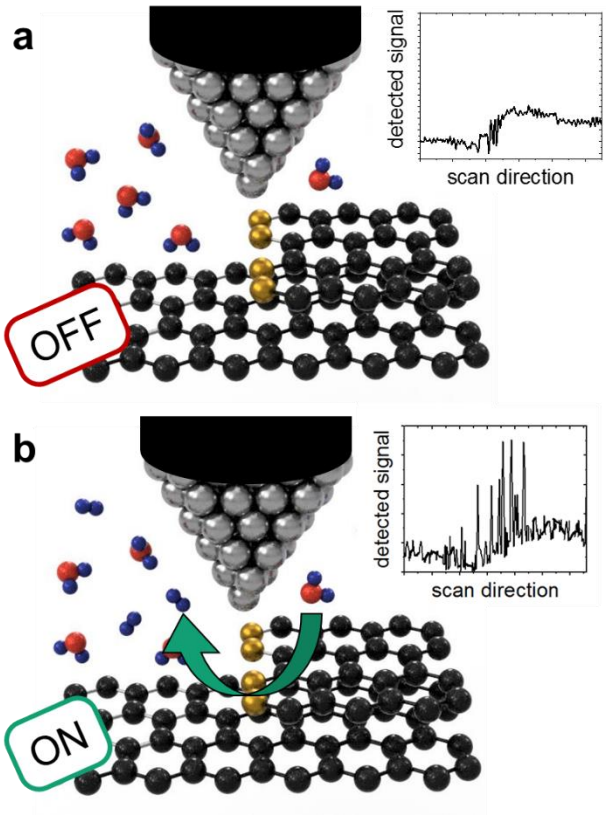

Figure 2. Working principle of n-EC-STM. Due to the influence of surface reactions on the tunnelling barrier properties (see main text and also Supplementary Material for details), different fluctuations in the recorded STM signal can be detected if the reaction is b, turned on compared to a, turned off. Since the noise features are particularly distinct at active compared to inactive sites, 'noise measurements' constitute a powerful tool for the in-situ identification of catalytically active centres. Carbon atoms of the graphite lattice are coloured in black, active carbon atoms in gold, oxygen atoms in red, hydrogen atoms in blue, and the tip atoms in silver.

the noise level of the signal is observed (Figure 2b). Over inactive sites, the observed noise level increase is fairly low. The most distinct increase in the noise level can be localized at the active centres. Distinguishing these variations in the recorded signal serves as a powerful tool to identify active catalytic sites. Setting the HOPG sample potentials such that a reaction is hindered will be labelled as 'off'. Accordingly, setting the electrode potential in a range, where the HER takes place will be referred to as 'on'. Said ranges are set to the regions (I) and (IV) in Figure 1 for 'on' and 'off', respectively.

In order to localize active sites on basal and/or edge planes, large-scale n-EC-STM measurements were performed as an overview. Figure 3 shows a single step edge marked with a white line to guide the eye. When comparing 'reaction on' (Figure 3b) to 'reaction off' (Figure 3a), distinct spots show an increased noise level, i.e. a yellowish colour. The spots are marked with white arrows in the figure. Below the n-EC-STM images, two line scans (red, black lines) are included at the same positions for 'on' and 'off'. The step edge is marked with a dotted line. For reaction 'off', the two line scans are similar. For reaction 'on', the position of the active site (red line) can be identified from the sharp spike in the tunnelling current, which is absent for inactive sites (black line). From both the EC-STM images and corresponding line scans, we assume that the active sites on HOPG are located near step edges. Nonetheless, in order to exclude any active sites being located at terraces, Figure 3c,d show two measurements across the same terrace, comparing reaction 'off' and 'on'. As expected, both images show similar tunnelling currents, and no distinct noise features appear, thus confirming our hypothesis.

After the initial indication that the active centres are located near step edges, we further increased the resolution of the n-EC-STM measurements. Note that the images in Figure 4 were FFT filtered to highlight the noise originating from the electrocatalytic processes. In this way of depiction, sites showing a comparatively high noise level in the as-recorded image show a comparatively high intensity after the FFT. The original images can be found in Figure S4 of the Supplementary Information. All three images in Figure 4 were recorded under reaction 'on' conditions. The direction of the line scans below the images are marked in the main image as lines of corresponding colour (black, red or blue).

Figure 4a shows a double step edge. The flat terraces next to it display an ordered honeycomb structure. Active sites can be located near the upper step edge as brighter spots (i.e., white colour) corresponding to a higher tunnelling current. In the exemplary line scans below the image, the positions of the two step edges are marked with grey lines. Near the first step edge, the active sites can be detected by a comparably higher tunnelling current (in the region $2\text{nm} < x < 3\text{nm}$).

Figure 4b shows an even higher resolved image of a step edge. Near the step edge, various active sites can be identified by their higher tunnelling current. In the line scans, a scan over an active (red line) is compared to an inactive (black line) site. From these data, we can assume that the active centres are not located exactly at the step edge, but rather in close vicinity to it. From the given image and line scans, we can hypothesize that the second row of C-atoms next to the step edge is the most active. However, due to the certain resolution limit of the experimental technique, we would also need to confirm this independently using e.g. theory methods, such as DFT calculations which will be presented later on (see Figure 5 and the corresponding explanation in the next paragraph).

In Figure 4c, besides the step edge, a region of defects within one of the terraces is also detected. Encircled in white, a misalignment of the honeycomb lattice can be observed. Active sites seem to be located within that area. In the line scans below the image, active (red line) and inactive (black line) sites are compared. Again, an increase in tunnelling current near the step edge can be observed indicating the position of the active sites. The blue line scan shows an active site located in the defective area, which can be identified by its comparably higher tunnelling current. Additional n-EC-STM data can be found in the Supplementary Information, Figure S2.

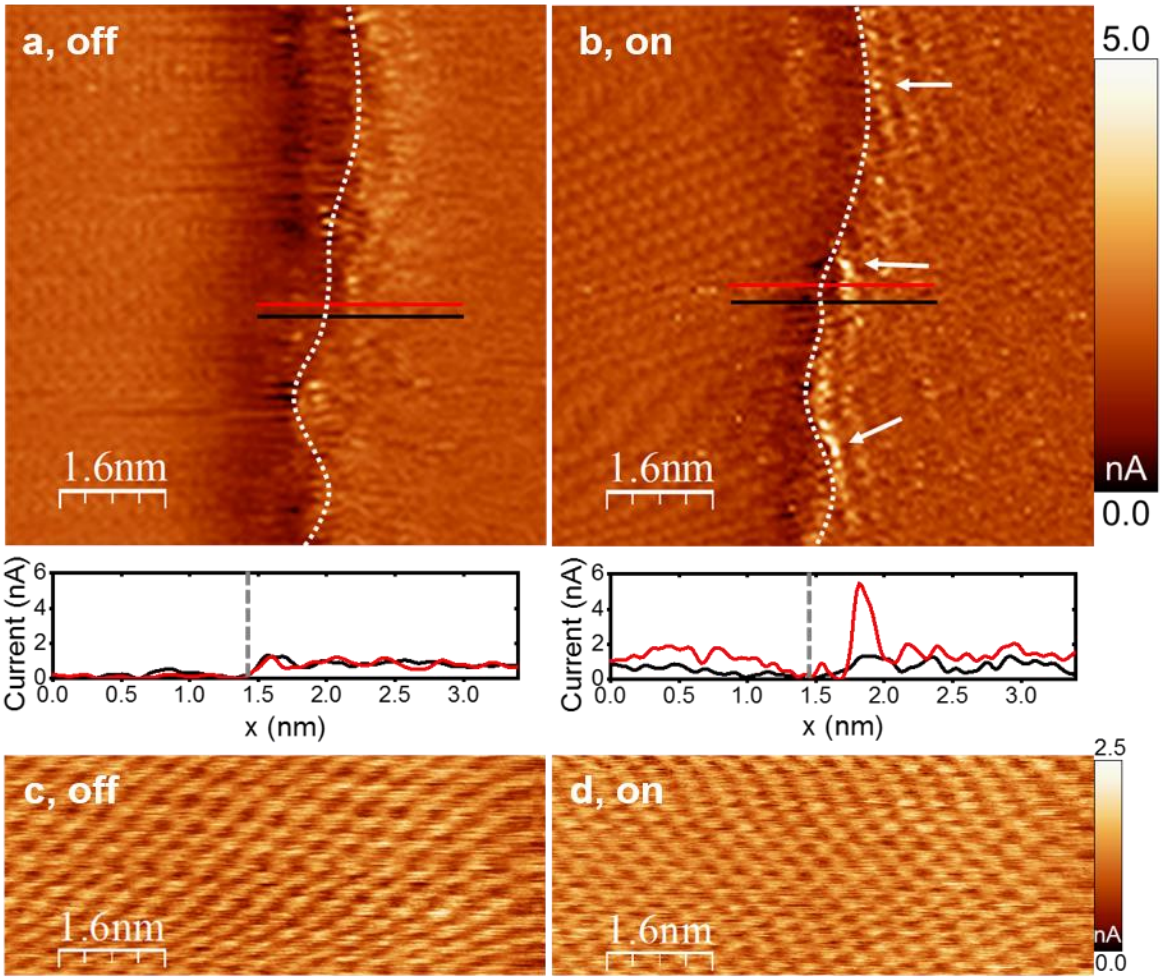

Figure 3. Large-scale n-EC-STM measurements. a, HER 'off'. A step edge can be identified and is marked by a white line as a guide to the eye. Below the image, two lines scans are given and the step-edge is marked by a grey line. b, Comparison to HER 'on'. Sites of higher noise level compared to HER 'off' can be identified in the vicinity of the step edge by their distinctly increased tunnelling current. These active sites are marked with arrows. The line scans below the image compare an inactive (black line) to an active (red line) site. A clear overshoot of the tunnelling current can be observed for the active site which is located near the step edge. In addition, defect-free terraces are shown for reaction c, 'off' and d, 'on'. No increase in noise level can be observed in either case. Therefore, we assume defect-free terraces to be inactive.

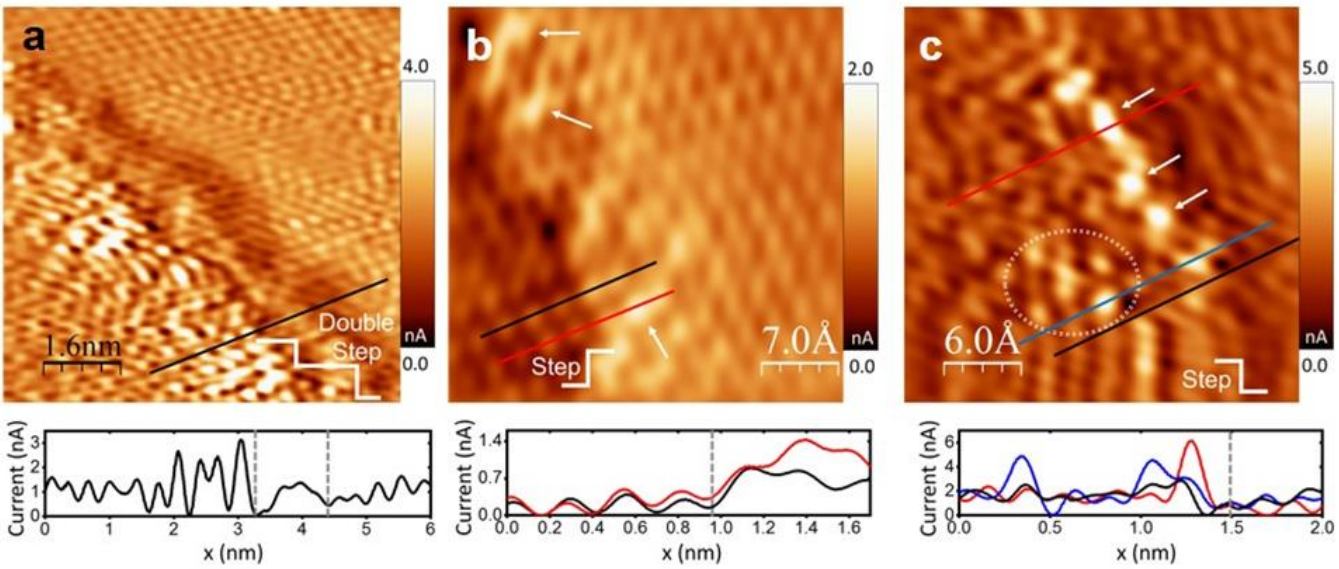

Figure 4. High-resolution n-EC-STM measurements on HOPG for HER 'on' conditions. All images were processed with FFT, see the raw data in Figure S4 of the Supporting Information. The position of the line scans below the images are marked in the main image as lines of corresponding color (black, red or blue). a, Active sites which show the highest tunneling currents (white color) are located in the vicinity of a step edge. In addition, the line scan confirms that the sites of the highest tunneling current are indeed located near the step edge (marked by a gray line). b, Active sites being detected with even higher resolution confirming their location near step edges. The line scans below indicate the second honeycomb away from the step edge being active. c, Active sites detected near the defective area, i.e., a deviation from the perfectly ordered carbon lattice (marked by white circle). The line scan below compares an inactive (black) to an active (red) step edge. Besides, the noise level increase at the defect sites is shown in blue.

In conclusion, these high-resolution images confirm that the active sites for the HER in acidic medium are located near defective and edge sites.

To complement our experimental observations with theoretical calculations, we modelled the HER on a variety of sites at pristine graphene and defective layers using structural motifs like pentagons, heptagons and octagons, C vacancies, armchair and zigzag edges (see the specific details in the Methods section and in the Supplementary Information). Two types of unit cells were considered: (i) a pristine graphene layer where all carbon atoms are arranged in hexagons ($cell_1$) and (ii) a layer containing also pentagons, heptagons and octagons ($cell_2$). We also introduced C divacancies and hydrogen-passivated step edges in those two cells, as shown in Figures S5-S11. In doing so, we are able to study a wide variety of defects that may be present in graphene[49] and in HOPG. Figure 5 shows the predicted HER overpotentials as a function of the free energy of adsorption of hydrogen. The volcano-shaped curve has a maximum at $\Delta G_H = 0$ eV, attesting to a Sabatier-type electrocatalytic process wherein optimal binding implies optimal catalytic performance and vice versa.[38,50] The shaded area in Figure 5 is located in the adsorption energy range of -0.5 to 0.5 eV. This is the low-overpotential region, as the active sites have HER overpotentials (η_{HER}) up to 0.5 V.

Carbon atoms at pristine terraces are fully coordinated and, therefore, bind hydrogen too weakly ($\Delta G_H \approx 2$ eV), which makes them inactive for the HER at practical potentials. The creation of defects in most cases lowers the HER overpotential by making the hydrogen adsorption energies stronger. For instance, the adsorption energies of hydrogen on a layer wherein pentagons, heptagons and octagons coexisting with hexagons are stronger by 0.6-1.3 eV compared to the pristine graphene.

Furthermore, there is a wide distribution of theoretical HER overpotentials around the step edges in several cases, with considerable differences with respect to the pristine terraces. As shown in Figure 5b-c, the lowest overpotentials are found for sites I-V, located at the step edges, C-vacancies and their proximities. Judging by Figure 5a and Figures S5-S11 of the Supplementary Information, we conclude that under-coordination is a necessary yet insufficient condition for HER activity on HOPG.

In other words, the most active sites are all located at or next to the defects, but not all calculated defect structures were active. Factors such as strain and buckling of the carbon networks around the sites probably influence the adsorption energies of hydrogen as well; further analysis is necessary. When comparing the DFT calculations to the STM experiments, it is important to point out that the potential values applied versus the Pt quasi-reference electrode in the experiment and the potential versus the computational hydrogen electrode are not equal. Since the Pt wire is only a quasi-reference electrode, there is no well-defined equilibrium potential. Therefore, it is also not possible to give a value for the applied overpotential during the measurements. We can, thus, only assume that the sample potentials applied for reaction 'on' in the EC-STM measurements are located in the area indicated as 'lower overpotential' in Figure 5. From the experimental findings, we can only assume that differences in the tunnelling current

intensity of active sites (Figure 3 and Figure 4) arise from differences in HER activity of different kinds of defects as revealed by DFT. Besides, we can also observe that not all sites near the step edges are active.

4. Discussion

The n-EC-STM measurements and DFT calculations corroborate the view that the most active sites on HOPG for HER in acidic medium are located at or near C-vacancies and step edges. Our findings on these well-defined surfaces are in accordance with earlier measurements on less defined high surface area electrodes, where authors reported that a high number of edge sites increases the performance of graphene for HER.[20,51] In this regard, defective graphene, derived from the removal of nitrogen atoms in N-doped graphene, can outperform its pristine and N-doped counterparts.[51] Moreover, the calculations suggest that deviations from the regular ring structure may increase the catalytic performance.[22] While there is some consensus on the activity of step edges[20,51], researchers still debate whether basal planes contain active sites[18,19]. Since we do not observe any activity of the basal planes during the HER, we can assume that either these centres deactivate faster than our measurements can detect them or that they are not active at all, as suggested by the DFT calculations for pristine graphene. Conversely, we show that even in the absence of metal heteroatoms, carbon can show activity for H_2 evolution at the active sites near defects or step edges. Due to the herein achieved resolution of the active centres on HOPG, we are optimistic that it is possible to extend n-EC-STM to modified (doped) carbon materials, thereby enabling the in-situ identification of their active sites.

5. Conclusion

In this study, we used n-EC-STM as valuable tool to in-situ detect active sites for the HER on carbon-based HOPG catalysts. We visualized the active centres located near edges and other defects with atomic resolution. DFT calculations also showed that step edges, C-vacancies and their vicinities are the most active sites for the HER on HOPG. We corroborate earlier hypotheses that the catalytic performance of carbon-based materials should increase with the number of edges and defects. We hence substantiate the heuristic notion that in order to prevent undesired H_2 evolution in supercapacitors, batteries and N_2- or CO_2-reducing electrolysers, synthetic chemists should produce high-surface area C-materials with minimum amount of under-coordinated defects. Additionally, we offer pathways to optimize carbon-based catalysts for hydrogen evolution.

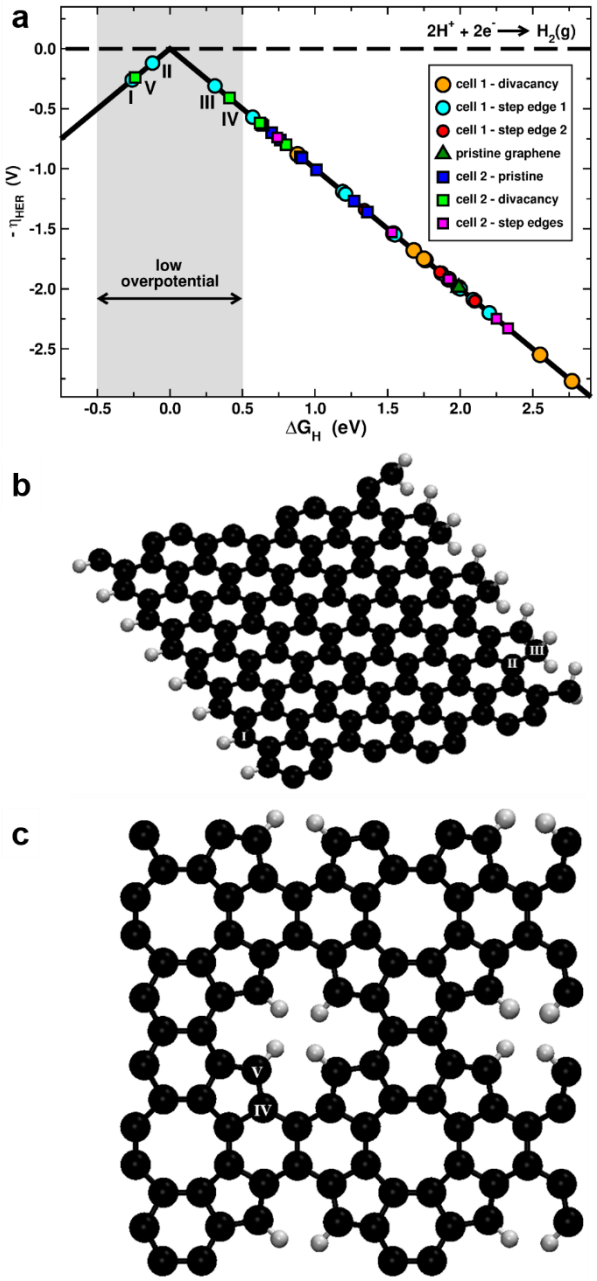

Figure 5. Computational analysis of hydrogen adsorption energies on pristine and defective graphene. a, Overpotentials for the HER as a function of the hydrogen adsorption energy. Data are provided for different sites at pristine graphene and two types of cells ($cell_1$ and $cell_2$). In $cell_1$ carbon atoms are arranged solely as hexagons, whereas $cell_2$ also contains pentagons, heptagons, octagons, and a carbon divacancy passivated by hydrogen. The dashed line marks the equilibrium potential; and the most active sites are located within the gray area. b, The most active sites on $cell_1$ (sites I-III). c, Most active sites on $cell_2$ (sites IV-V). All active sites in $cell_1$ and $cell_2$ are shown in the SI, Figures S5-S11.

Author Contributions

The manuscript was written through contributions of all authors. All authors have given approval to the final version of the manuscript. ‡RMK and RWH contributed equally.

Conflicts of interest

There are no conflicts to declare.

Acknowledgements

We thank Prof. Plamen Atanassov (University of California, Irvine, USA) and Dr. Jun Maruyama (Osaka Research Institute of Industrial Science and Technology, Japan) for fruitful discussion regarding some experimental results. RMK, RWH and ASB acknowledge the financial support from German Research Foundation (DFG), in the framework of the projects BA 5795/4-1 and BA 5795/3-1, and under Germany´s Excellence Strategy–EXC 2089/1–390776260, cluster of excellence 'e-conversion'. ASB acknowledges funding provided from the European Union's Horizon 2020 research and innovation programme under grant agreement HERMES No 952184. FCV acknowledges financial support from Spanish MICIUN through RTI2018-095460-B-I00 and María de Maeztu (MDM-2017-0767) grants and a Ramón y Cajal research contract (RYC-2015-18996), and also from Generalitat de Catalunya (grants 2017SGR13 and XRQTC). The use of supercomputing facilities at SURFsara was sponsored by NWO Physical Sciences, with financial support by NWO.

References

1 L. Wang, Z. Sofer and M. Pumera, *Nanoscale*, 2019, **11**, 11083.
2 M. Bernt, A. Siebel and H. A. Gasteiger, *J. Electrochem. Soc.*, 2018, **165**, F305.
3 M. He, K. Fic, E. Frąckowiak, P. Novák and E. J. Berg, *Energy Environ. Sci.*, 2016, **9**, 623.
4 D. Strmcnik, I. E. Castelli, J. G. Connell, D. Haering, M. Zorko, P. Martins, P. P. Lopes, B. Genorio, T. Østergaard, H. A. Gasteiger, F. Maglia, B. K. Antonopoulos, V. R. Stamenkovic, J. Rossmeisl and N. M. Markovic, *Nat. Catal.*, 2018, **1**, 255.
5 N. Lazouski, M. Chung, K. Williams, M. L. Gala and K. Manthiram, *Nat. Catal.*, 2020, **3**, 463.
6 A. K. Geim and K. S. Novoselov, *Nanosci. Nanotechnol.*, 2009, **11**, 183.
7 A. Ambrosi, C. K. Chua, N. M. Latiff, A. H. Loo, C. H. an Wong, A. Y. S. Eng, A. Bonanni and M. Pumera, *Chem. Soc. Rev.*, 2016, **45**, 2458.
8 Y. Zheng, Y. Jiao, L. H. Li, T. Xing, Y. Chen, M. Jaroniec and S. Z. Qiao, *ACS Nano*, 2014, **8**, 5290.
9 a) B. R. Sathe, X. Zou and T. Asefa, *Catal. Sci. Technol.*, 2014, **4**, 2023; b) A. Roy, D. Hursán, K. Artyushkova, P. Atanassov, C. Janáky and A. Serov, *Appl. Catal. B*, 2018, **232**, 512; c) C. Hu and L. Dai, *Adv. Mater.*, 2017, **29**; d) K. Jayaramulu, J. Masa, O. Tomanec, D. Peeters, V. Ranc, A. Schneemann, R. Zboril, W. Schuhmann and R. A. Fischer, *Adv. Funct. Mater.*, 2017, **27**, 1700451.
10 Y. Ito, W. Cong, T. Fujita, Z. Tang and M. Chen, *Angew. Chem.*, 2015, **127**, 2159.
11 a) D. Geng, Y. Chen, Y. Chen, Y. Li, R. Li, X. Sun, S. Ye and S. Knights, *Energy Environ. Sci.*, 2011, **4**, 760; b) D. W. Chang, H.-J. Choi and J.-B. Baek, *J. Mater. Chem. A*, 2015, **3**, 7659; c) S. Dresp, F. Luo, R. Schmack, S. Kühl, M. Gliech and P. Strasser, *Energy Environ. Sci.*, 2016, **9**, 2020; d) J. P. Paraknowitsch and A. Thomas, *Energy Environ. Sci.*, 2013, **6**, 2839.
12 Z. Yang, Z. Yao, G. Li, G. Fang, H. Nie, Z. Liu, X. Zhou, X. Chen and S. Huang, *ACS Nano*, 2012, **6**, 205.
13 J. Masa, W. Xia, M. Muhler and W. Schuhmann, *Angew. Chem.*, 2015, **54**, 10102.
14 a) T. Y. Ma, S. Dai, M. Jaroniec and S. Z. Qiao, *Angew. Chem.*, 2014, **53**, 7281; b) Y. Zhao, R. Nakamura, K. Kamiya, S. Nakanishi and K. Hashimoto, *Nat. Commun.*, 2013, **4**, 2390; c) J. Maruyama, S. Maruyama, T. Fukuhara, H. Mizuhata, S. Takenaka, A. Yoshida and K. Miyazaki, *J. Electrochem. Soc.*, 2020, **167**, 60504;
15 L. Zhang, Q. Xu, J. Niu and Z. Xia, *Phys. Chem. Chem. Phys.*, 2015, **17**, 16733.
16 D. A. C. Brownson, D. K. Kampouris and C. E. Banks, *Chem. Soc. Rev.*, 2012, **41**, 6944.
17 R. L. McCreery, *Chem. Rev.*, 2008, **108**, 2646.
18 S. C. S. Lai, A. N. Patel, K. McKelvey and P. R. Unwin, *Angew. Chem.*, 2012, **124**, 5501.
19 T. J. Davies, M. E. Hyde and R. G. Compton, *Angew. Chem. Int. Ed.*, 2005, **44**, 5121.
20 H. Wang, X.-B. Li, L. Gao, H.-L. Wu, J. Yang, Le Cai, T.-B. Ma, C.-H. Tung, L.-Z. Wu and G. Yu, *Angew. Chem.*, 2018, **130**, 198.
21 a) Li Tao, Q. Wang, S. Dou, Z. Ma, J. Huo, S. Wang and L. Dai, *ChemComm*, 2016, **52**, 2764; b) J. C. Byers, A. G. Güell and P. R. Unwin, *J. Am. Chem. Soc.*, 2014, **136**, 11252;
22 M. Titirici, *Nat. Catal.*, 2019, **2**, 642.
23 a) N. Holmberg and K. Laasonen, *J. Phys. Chem. Lett.*, 2015, **6**, 3956; b) Y. Jia, L. Zhang, L. Zhuang, H. Liu, X. Yan, X. Wang, J. Liu, J. Wang, Y. Zheng, Z. Xiao, E. Taran, J. Chen, D. Yang, Z. Zhu, S. Wang, L. Dai and X. Yao, *Nat. Catal.*, 2019, **2**, 688.
24 a) I. Matanovic, K. Artyushkova, M. B. Strand, M. J. Dzara, S. Pylypenko and P. Atanassov, *J. Phys. Chem. C*, 2016, **120**, 29225; b) D. Zeng, X. Yu, Y. Zhan, L. Cao, X. Wu, B. Zhang, J. Huang, Z. Lin, F. Xie, W. Zhang, J. Chen, W. Xie, W. Mai and H. Meng, *Int. J. Hydrog. Energy*, 2016, **41**, 8563; c) D. Guo, R. Shibuya, C. Akiba, S. Saji, T. Kondo and J. Nakamura, *Science*, 2016, **351**, 361.
25 J. H. K. Pfisterer, Y. Liang, O. Schneider and A. S. Bandarenka, *Nature*, 2017, **549**, 74.
26 L. A. Nagahara, T. Thundat and S. M. Lindsay, *Rev. Sci. Instrum.*, 1989, **60**, 3128.
27 Y. Liang, C. Csoklich, D. McLaughlin, O. Schneider and A. S. Bandarenka, *ACS Appl. Mater. Interfaces*, 2019, **11**, 12476.
28 Y. Liang, D. McLaughlin, C. Csoklich, O. Schneider and A. S. Bandarenka, *Energy Environ. Sci.*, 2019, **12**, 351.

29 E. Mitterreiter, Y. Liang, M. Golibrzuch, D. McLaughlin, C. Csoklich, J. D. Bartl, A. Holleitner, U. Wurstbauer and A. S. Bandarenka, *npj 2D Mater. Appl.*, 2019, **3**, 25.
30 R. W. Haid, R. M. Kluge, Y. Liang and A. S. Bandarenka, *Small Methods*, 2021, **5**, 2000710.
31 I. Horcas, R. Fernández, J. M. Gómez-Rodríguez, J. Colchero, J. Gómez-Herrero and A. M. Baro, *Rev. Sci. Instrum.*, 2007, **78**, 13705.
32 Kresse and Furthmüller, *Phys. Rev. B,* 1996, **54**, 11169.
33 G. Kresse and D. Joubert, *Phys. Rev. B*, 1999, **59**, 1758.
34 B. Hammer, L. B. Hansen and J. K. Nørskov, *Phys. Rev. B*, 1999, **59**, 7413.
35 H. J. Monkhorst and J. D. Pack, *Phys. Rev. B*, 1976, **13**, 5188.
36 J. K. Nørskov, J. Rossmeisl, A. Logadottir, L. Lindqvist, J. R. Kitchin, T. Bligaard and H. Jónsson, *J. Phys. Chem. B*, 2004, **108**, 17886.
37 D. R. Lide, *CRC handbook of chemistry and physics, 2003-2004. A ready-reference book of chemical and physical data*, CRC Press, Boca Raton, Fla., 84th edn., 2003.
38 J. K. Nørskov, T. Bligaard, A. Logadottir, J. R. Kitchin, J. G. Chen, S. Pandelov and U. Stimming, *J. Electrochem. Soc.*, 2005, **152**, J23.
39 S. Grimme, J. Antony, S. Ehrlich and H. Krieg, *J. Chem. Phys.*, 2010, **132**, 154104.
40 K. Mathew, R. Sundararaman, K. Letchworth-Weaver, T. A. Arias and R. G. Hennig, *J. Chem. Phys.*, 2014, **140**, 84106.
41 A. Rendón-Calle, S. Builes and F. Calle-Vallejo, *Appl. Catal. B*, 2020, **276**, 119147.
42 A. Kraft, *Int. J. Electrochem. Sci.*, 2007, 355.
43 J. Maruyama and I. Abe, *Electrochim. Acta*, 2001, **46**, 3381.
44 C. Barbero, J. J. Silber and L. Sereno, *J. Electroanal. Chem. Interf. Electrochem.*, 1988, **248**, 321.
45 M. Hugelmann and W. Schindler, *Surf. Sci.*, 2003, **541**, 643-L648.
46 M. Hugelmann and W. Schindler, *J. Electrochem. Soc.*, 2004, **151**, E97.
47 a) J. Halbritter, G. Repphun, S. Vinzelberg, G. Staikov and W. J. Lorenz, *Electrochim. Acta*, 1995, **40**, 1385; b) G. Engelmann, J. Ziegler and D. Kolb, *Surf. Sci.*, 1998, **401**, L420.
48 a) G. Nagy and T. Wandlowski, *Langmuir*, 2003, **19**, 10271; b) G. Binnig, H. Fuchs and E. Stoll, *Surf. Sci. Lett.*, 1986, **169**, L295.
49 F. Banhart, J. Kotakoski and A. V. Krasheninnikov, *ACS Nano*, 2011, **5**, 26.
50 a) M. T. Koper, *J. Electroanal. Chem.*, 2011, **660**, 254; b) M. D. Pohl, S. Watzele, F. Calle-Vallejo and A. S. Bandarenka, *ACS Omega*, 2017, **2**, 8141.
51 Y. Jia, L. Zhang, A. Du, G. Gao, J. Chen, X. Yan, C. L. Brown and X. Yao, *Adv. Mater.*, 2016, **28**, 9532.